TECHNICAL ARTICLE

Structure and Properties of a High-Entropy Ti-Zr-Hf-Ni-Co-Cu Alloy Obtained by Mechanical Alloying and Spark Plasma Sintering

N. G. Razumov[1] · T. Yu. Makhmutov[1] · A. Kim[1] · I. S. Goncharov[2] · N. E. Ozerskoi[1] · A. O. Silin[1] · A. K. Mazeeva[1] ·
A. A. Popovich[1]

Abstract

In this paper, the synthesis of a high-entropy Ti-Zr-Hf-Ni-Co-Cu alloy (HEA) by powder metallurgy (PM) methods was investigated. This alloy is prospective from high-temperature shape memory effect point of view. The composition of $(TiZrHf)_{50}Ni_{25}Co_{10}Cu_{15}$ was chosen for the study as it promised to show high functional properties. In order to synthesize the alloy, spark plasma sintering (SPS) of its spherical powder was used. The spherical powders were previously obtained by mechanical alloying of elemental powders and subsequent plasma spheroidization (PS). It was shown that the structure of the bulk samples consisted of B2-TiNi-type austenite, low-melting eutectic CuZr and C15 Laves phase. The eutectic, which precipitates during the SPS process, prevents deforming spherical particles and leads to low mechanical properties since the material does not work as a monolith one. The compressive ultimate stress was 425 ± 15 MPa. However, the hardness of more than 600 HV that is higher than for any binary intermetallic compounds consisted of the HEA elements promises good prospects of PM methods for production of such alloys. For this purpose, a problem of high oxygen content that also results in the liability to brittle fracture should be solved.

Keywords High-entropy alloy · Mechanical alloying · Plasma spheroidization · Spark plasma sintering · Microstructure

Introduction

For the last 15 years, a new direction has been actively developing in the creation of structural materials based on high-entropy alloys (HEA) [1–5]. According to the currently accepted basic definition, these alloys are consisting of at least five components with the content in the range of 5–35 at.% [2]. Despite the multicomponent nature of most HEAs, even alloys with twenty elements mainly consist of a single phase based on the face-centered, hexagonal close-packed or body-centered cubic lattice [1]. However, the formation of some inter-dendritic phases during production of HEA by various melting methods makes alloys with a very large number of elements brittle and unsuitable for use in practice [1]. At the same time, the experimental data available at the moment allows to distinguish five-component compositions that have a single-phase structure and demonstrate unique properties compared to conventional alloys with one or two main components [1]. High-entropy alloys have higher wear-resistance, corrosion-resistance, and strength properties [3, 6–10]. Solid solutions based on five or more components will tend to be more stable at elevated temperatures due to the large entropies of mixing [11, 12].

Due to a huge number of possible combinations of elements in the HEAs, the areas of their potential application are also very wide. Recently, researchers have begun to show interest in the creation of high-entropy alloys with shape memory effect (SME). High-entropy Ti-Zr-Hf-Ni-Co-Cu alloys were studied in [13–16]. Such alloys are pseudo-binary intermetallic compounds based on TiNi which is well known for its shape memory effect [17–20] and is already very widely used in practice, in particular, in medicine [21, 22]. The addition of elements that are highly soluble in titanium (Zr, Hf) or nickel (Co, Cu) [23–25] preserves the crystal structure of TiNi. But at the same time, it allows

✉ A. K. Mazeeva
  mazeevaalina@gmail.com

[1] Institute of Machinery, Materials and Transport,
  Peter the Great St. Petersburg Polytechnic University,
  Polytechnicheskaya, 29, Saint-Petersburg,
  Russian Federation 195251

[2] Department of Mechanical Engineering, Politecnico di
  Milano, Via Privata Giuseppe La Masa 1, 20156 Milan, Italy

to vary the temperatures of the martensitic transformation (MT) responsible for the exhibition of SME in a wide range since the use of TiNi is limited to a maximum temperature of 100 °C [20, 23, 26–29]. It also allows to improve their mechanical characteristics [23, 30–33]. At the same time, the application of the basic principle of high-entropy alloys (equiatomic composition) provides achieving better functional properties compared to non-equiatomic compositions [31].

In [13–16], Ti–Zr–Hf–Ni–Co–Cu alloys were obtained by multiple remelts using conventional methods of arc and vacuum arc melting, and sometimes the ingots were subjected to subsequent rolling. These methods make it possible to obtain ingots of a given chemical composition [34]. At the same time, even the use of these methods does not guarantee complete uniformity of the chemical composition over the volume of the ingot and the content of impurities at the same level and can lead to a large variation in the MT temperatures of ingots of the same composition obtained at different production [14, 35]. Another problem of these methods is the presence of a large number of refractory elements in the HEA which makes the melting process very energy-intensive and requires the use of special high-temperature equipment. To partially solve these problems, it is possible to use the methods of powder metallurgy (PM) which allows to avoid heating to the melting points of the components and to use lower temperatures. One of the modern methods of PM is spark plasma sintering (SPS) which consists of the combined action of external pressure and passing a pulsed pulsating current through the powder that intensifies sintering. In [36–40], the possibility of using SPS to obtain compact samples with a relative density about 99% from powders of refractory HEAs was shown. The general trend in these works is to refine the grain in comparison to ingots obtained by conventional methods that leads to a significant increase in yield strength, ultimate strength and hardness but also reduces the plastic properties. Also for each composition, it is necessary to select peculiar temperature and time modes to ensure a single-phase structure in the HEA.

At the moment, there are quite a few works devoted to the production and study of functional HEA, in particular, those that can exhibit the shape memory effect obtained by PM methods.

The aim of this work was to study the process of spark plasma sintering of a high-entropy Ti–Zr–Hf–Ni–Co–Cu alloy powder obtained by mechanical alloying of elemental powders with subsequent plasma spheroidization and to analyze its effect on the chemical composition, structure and mechanical properties of the HEA.

Materials and Methods

Spherical powders of high-entropy $(TiZrHf)_{50}Ni_{25}Co_{10}Cu_{15}$ alloy obtained by mechanical alloying with subsequent plasma spheroidization were used for research. Mechanical alloying (MA) is one of the most technologically advanced methods of powder metallurgy for the production of powders of various compositions. It is carried out due to intensive mechanical impact on the initial powder material resulting in the element penetration into each other, up to chemical interaction between them. The rotation speed of the working parts of the mill and the impact time are the main technological parameters that determine the energy characteristics and intensity of the process.

Elemental powders of Ti (99.5% purity) with the particle size of 100–150 μm, Zr (99.0% purity) with the average particle size of 10 μm, Hf (99.9% purity) with the particle size of 40–60 μm, Ni (99.5% purity) with the particle size of 71–250 μm, Co, Cu (99.5% purity) with the particle size of up to 100 μm were used as initial materials.

Mechanical alloying was carried out using the Fritsch Pulverisette 4 vario-planetary mill (Germany) in a high-purity argon atmosphere. The ratio of the mass of the milled material to the mass of the milling balls was 1:20, and the rotation speed of the planetary disk/cup was 200/-400 rpm. The MA time was 5–20 h, the diameter of the milling balls was 8–10 mm, and the weighted average diameter was 8.6 mm.

Plasma spheroidization was performed by using Tek-15 unit (Tekna Plasma Systems Inc.). The process parameters were as follows: plasma torch power—15 kW; powder feed rate—35–40 g/min; plasma-forming gas is argon-hydrogen mixture, gas consumption: Ar-50 slpm, H_2-3.5 slpm; feed point—0 mm (in the center of the induction coil).

Spark plasma sintering was performed by using FCT HPD 25 (FCT Systeme GmbH, Germany). Sintering was carried out in graphite molds Ø80 mm at the temperature of 900 °C. The sintering temperature was selected based on calculated phase diagrams. The sintering load was 250 kN applied after heating the sample to 900 °C. The heating rate was 50 °C/min, and the load raising rate was 125 kN/min. The holding time at the temperature of 900 °C and the pressure of 250 kN was 2 min. Time of cooling from 900 to 400 °C was 1 min.

The phase composition was determined by x-ray phase analysis by using Bruker D8 Advance unit in Cu $K\alpha$ radiation ($\lambda = 0.15418$ nm). Further processing of the data was carried out by using the Rietveld method with Bruker Diffrac Plus Topas program. The morphology, structure, chemical composition and element distribution over the cross section of the samples were studied using a Tescan Mira 3 LMU scanning electron microscope equipped

with attachment for energy-dispersive spectral analysis. The porosity of the samples after SPS was determined by hydrostatic weighing. The hardness of the samples was determined by the standard Vickers scale method.

Results

Figures 1 and 2 show maps of component distribution by volume of powder particles after mechanical alloying
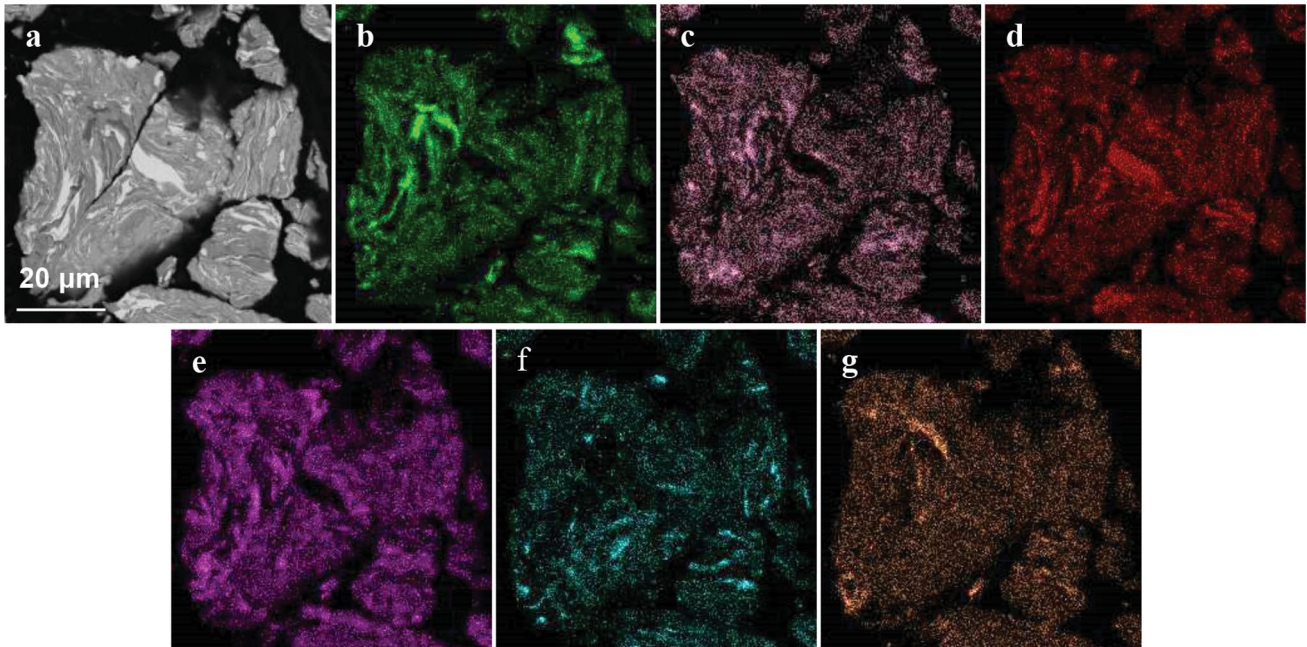

Fig. 1 Component distribution in the powder particles of $(TiZrHf)_{50}Ni_{25}Co_{10}Cu_{15}$ composition after MA for 5 h (rotation speed of planetary disk-200 rpm, grinding cup-400 rpm): (**a**) general appearance, (**b**) Ti, (**c**) Zr, (**d**) Hf, (**e**) Ni, (**f**) Co, (**g**) Cu
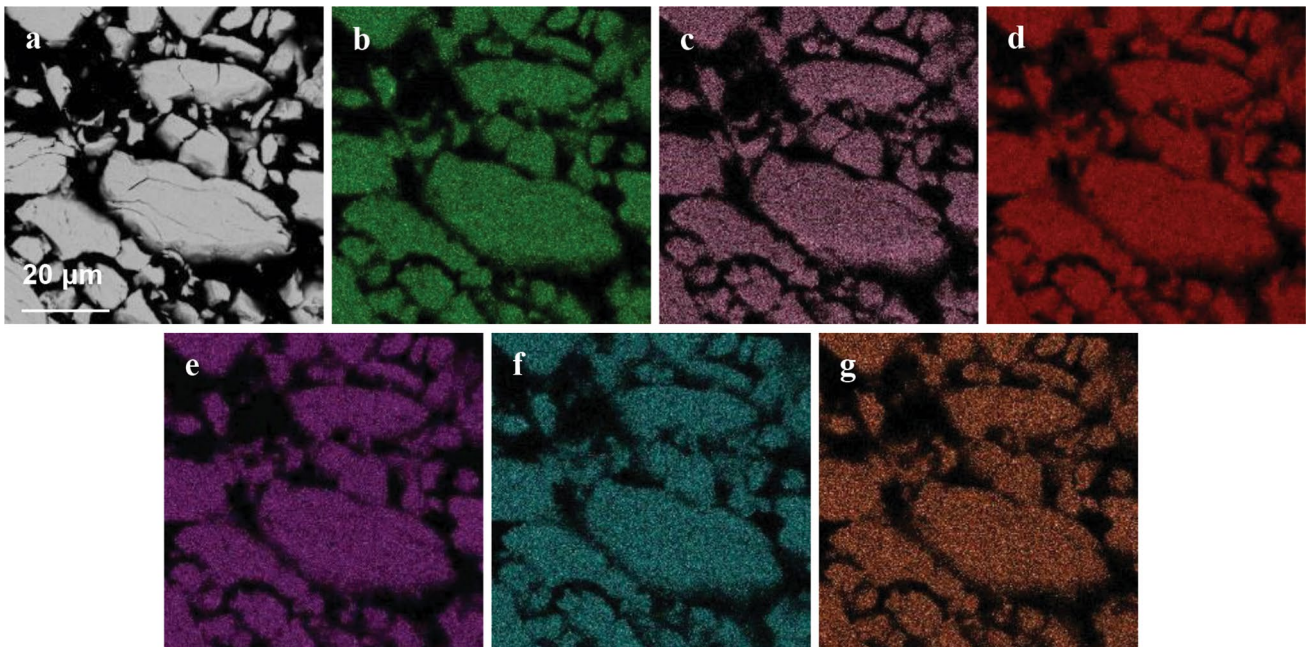

Fig. 2 Component distribution in the powder particles of $(TiZrHf)_{50}Ni_{25}Co_{10}Cu_{15}$ composition after MA for 20 h (rotation speed of planetary disk-200 rpm, grinding cup-400 rpm): (**a**) general appearance, (**b**) Ti, (**c**) Zr, (**d**) Hf, (**e**) Ni, (**f**) Co, (**g**) Cu

process during 5 and 20 h. At the beginning of the MA process due to intense plastic deformation, the particles of the initial powder are flattened and welded together to form a composite. It was found that the powder particles after 5 h of MA have a layered structure with a thickness of lamellae up to 60 µm. With an increase in the MA duration, the thickness of the lamellae decreases and reaches a size of less than 200 nm after 20 h of MA. But it is worth noting that the process of mutual dissolution of the elements of the initial composition differs from the interaction inherent for only plastic components since the initial elements used in this paper differ significantly in hardness and plasticity from each other. Powder particles consisting of plastic components (for example, Ti and Ni) are flattened and joined by mechanism similar to cold welding to form layered composites [41].

In a mixture of plastic and brittle components, the brittle particles are destroyed and then covered with plastic particles. The inclusions of the brittle components have a fragmentary shape. This situation can be seen in Fig. 2. With a further increase in MA duration, the main processes are homogenization of the chemical composition and interaction between the initial components leading to reduction of the free energy of the system. After 20 h of MA, the alloying elements are almost uniformly distributed over the volume of the powder and correspond to the initial chemical composition (Fig. 2). In addition, the brittle particles of Hf and Zr themselves are prone to intermetallic formation which is intensified with prolonged MA due to an increase in local temperatures and the time of their exposure. The brittle particles are gradually disintegrated with prolonged MA. The average particle size

after 20 h of MA was 30 µm. Maximum particle size was 90 µm.

Taking into account the ratio of the components sizes in the HEA it can be assumed that during mechanical alloying in this system diffusion mainly takes place at defects in the crystal lattice. It is widely believed that the rate of phase transformations during mechanical alloying also depends on diffusion mobility of the components. However, the coefficients of mutual diffusion and their change with temperature at a high concentration of point, linear and plane defects are not known. It is believed that they can be several orders of magnitude higher than the diffusion coefficients attributed to stationary conditions.

According to chemical composition analysis, it was shown that the confidence interval of deviation from the average composition in the powder particles after 5 h of MA is 10–25% that indicates a strong heterogeneity of the chemical composition of individual powder particles. With an increase in MA duration, the confidence interval of deviation decreases that indicates the alignment of the chemical composition for individual powder particles.

Due to intensive mechanical impact on the milled material, mechanical alloying also leads to a change in material structure by inducing a large quantity of defects which increases with increase in MA duration. It ultimately leads to the formation of an x-ray amorphous structure (Fig. 3).

As a result of the study of subsequent treatment in the flow of thermal argon-hydrogen plasma generated in a high-frequency plasma torch, experimental samples of HEA powders with various degrees of spheroidization were obtained (Fig. 4). The studies of the powder particle morphology powder have shown that the proportion of spheroidized

Fig. 3 Phase composition of $(TiZrHf)_{50}Ni_{25}Co_{10}Cu_{15}$ alloy after mechanical alloying in planetary mill (rotation speed of planetary disk-200 rpm, grinding cup-400 rpm)
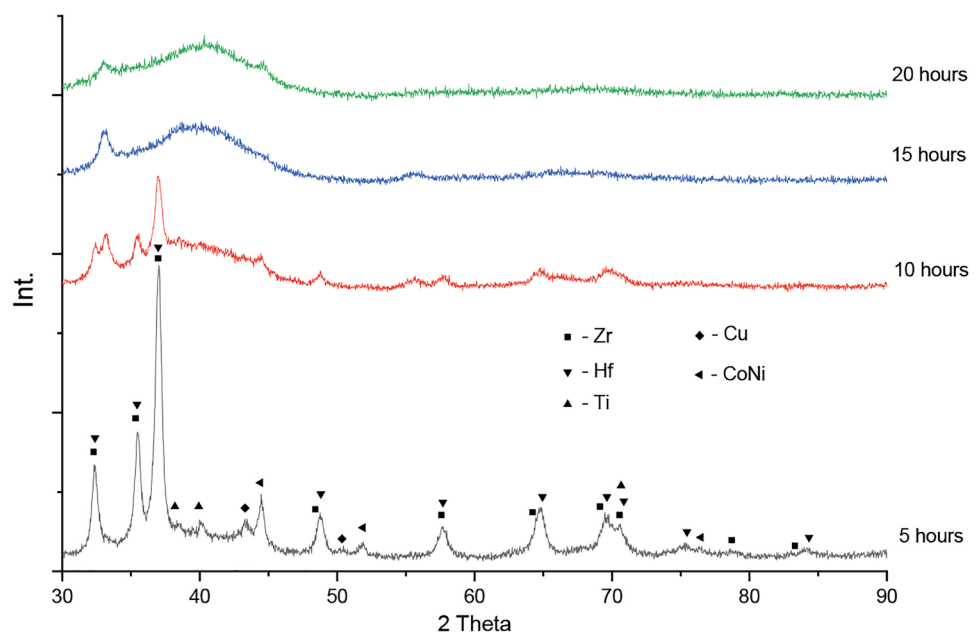
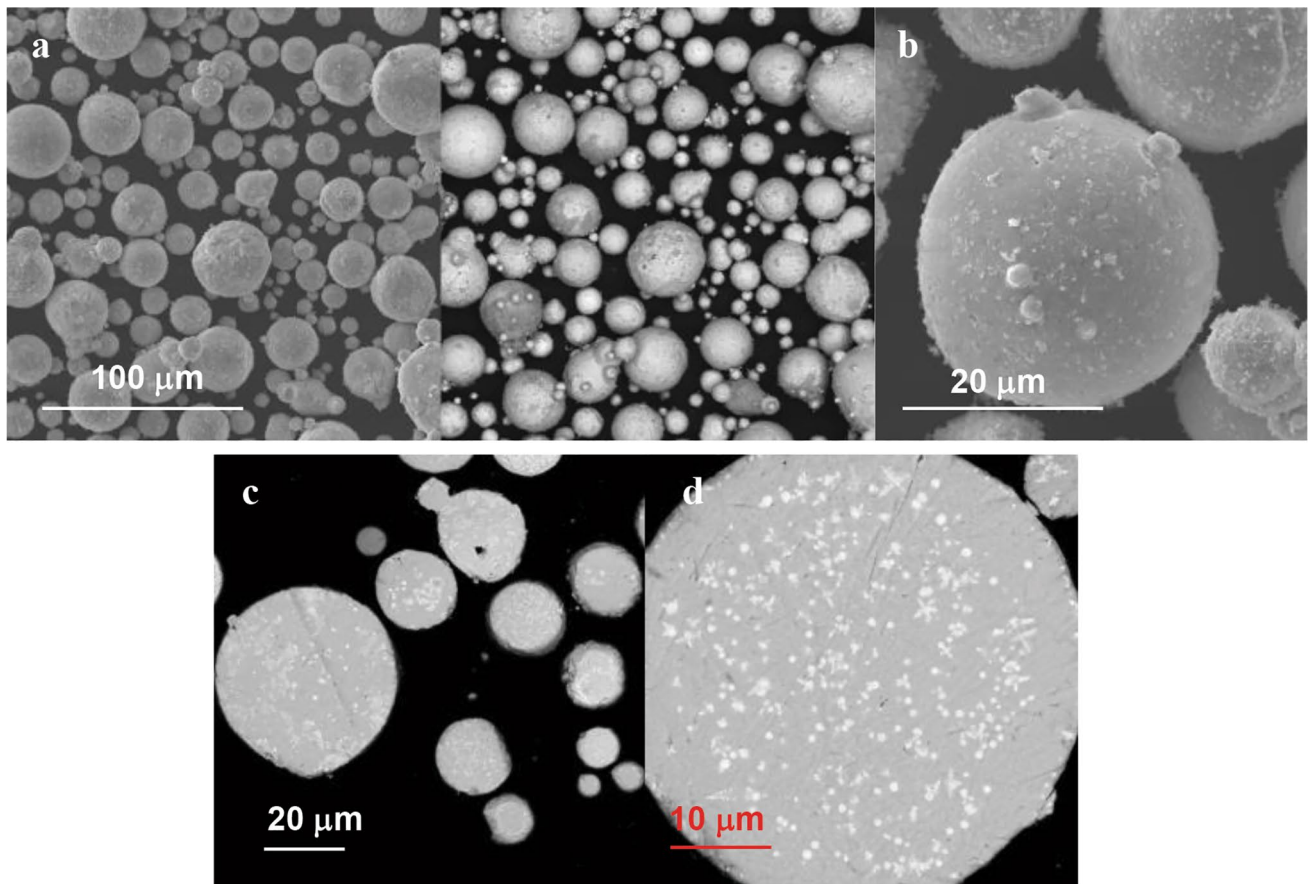**Fig. 4** Morphology (**a**, **b**) and structure (**c**, **d**) of $(TiZrHf)_{50}Ni_{25}Co_{10}Cu_{15}$ alloy powder particles after plasma spheroidization at the plasma unit power of 15 kW and the feed rate of 38 g/min at various magnifications : (**a**) 1000 × (SE and BSE); (**b**) 5000 ×; (**c**) 1000 × (**d**) 5000 ×

particles in the obtained powders is more than 95%. At the same time more than 85% of the particles have a spherical shape, less than 5% have an irregular shape, the rest ones have a rounded shape with a shape factor (the ratio of the largest dimension of a particle to the smallest one) of 1.2–2. Due to the presence of a large number of small particles in the initial powder, their partial evaporation occurs during plasma spheroidization, followed by condensation of the vapor as nanoparticles on the surface of the powder (Fig. 4b).

The initial temperature of the plasma is significantly higher than the boiling point of the material particles. When small metal particles are heated in a high-temperature gas flow, the temperature on their surface does not differ much from the temperature in their center. It means that evaporation occurs not due to overheating of the surface layer of the particles but as a result of evaporation of the smallest particles having time to heat up to the boiling point during their stay in the high-temperature zone. The resulting coating of submicron particles negatively affects the technological characteristics of the resulting powder. It reduces fluidity and increases the content of oxygen impurities due

to oxidation of submicron particles under contact with air. It is necessary to classify the initial powder to reduce the effect of submicron particle formation. The result of the classification is removing of submicron particles and then a narrow-fraction powder is processed. Figure 5 shows the data on the effect of different processing modes on the granulometric composition of the powders.

Analysis of $(TiZrHf)_{50}Ni_{25}Co_{10}Cu_{15}$ powder particle structure shows that the particles have a fine-grained structure with an average grain size of about 3 µm (Fig. 4). There are no micron-sized and submicron-sized pores in the cross sections of the particles. At large magnifications, the secondary phase is observed in the alloy. It differs from the base in contrast. A lighter shade indicates that the inclusions have a higher density in comparison to the base phase.

The component distribution maps showed that there was increased hafnium and zirconium content in the areas of secondary phase formation (Fig. 6).

The secondary phase precipitates are small enough for micro-x-ray spectral analysis. However, summarizing these results with the XRD results (Fig. 7), it can be assumed that the secondary precipitates are a mixture of hafnium and
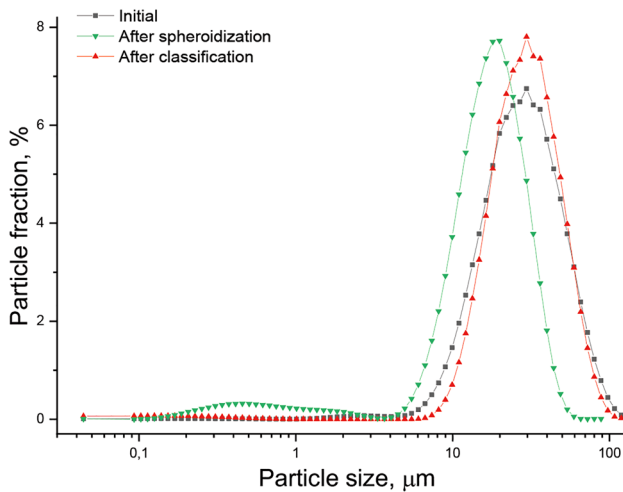
zirconium-based intermetallic compounds ($ZrHf_{0.302}$) and HfO_2 and ZrO_2 oxides which may be a result of impurities in the initial elemental powders.

Bulk samples of the HEA had the shape of disks with Ø80 mm and $h = 10$ mm and were obtained according to the selected SPS modes. The porosity of the resulting blanks is 1%. Figures 8 and 9 show the microstructure and component distribution over the cross section of the bulk sample. During sintering a low-melting point eutectic CuZr is evolved,

its melting point is 920 °C according to its phase diagram. The separation of the liquid phase prevents the deformation of the initial powder particles (Fig. 8). Thus, in the SPS process, compaction occurs not due to the interaction of particles with each other but due to the connecting with the low-melting point eutectic.

As a result, two-phase components are found in the bulk sample that differ in contrast. The gray matrix has a phase structure corresponding to B2-TiNi austenitic state, and the light gray precipitates corresponding to Laves phase. These data are confirmed by the XRD results (Fig. 7).

The average grain size of B2-austenite and Laves phase inclusions after SPS process is ~ 2–3 μm. The structure corresponds to the structure of the initial powder which was formed during the plasma spheroidization process. The main phase component in the samples after SPS and quenching in water after annealing at 1050 °C is the phase with the crystal lattice corresponding to B2-TiNi with the cell parameter $a = 3.1053$ Å after SPS and $a = 3.1112$ Å after quenching. In addition, there are lines corresponding to zirconium oxides ZrO, ZrO_2 and the Laves phase.

The x-ray lines of B2-austenite are asymmetric and have the shape of asymmetric doublets. The periods of the B2-lattice calculated from the coordinates of the singletons of each doublet of the same sample are identical within a very small error (3.0863–3.1112 Å). These observations lead to the conclusion that the B2-austenite is not a homogeneous phase but is separated into two phases (two

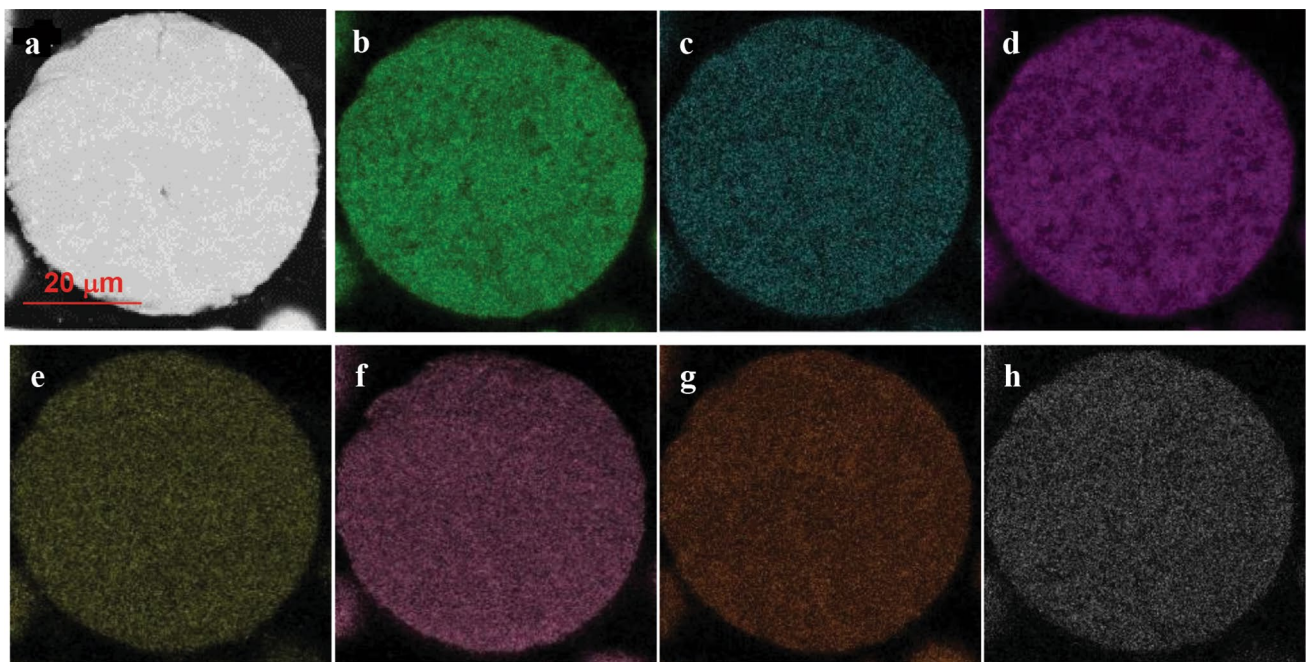Fig. 6 Component distribution maps in $(TiZrHf)_{50}Ni_{25}Co_{10}Cu_{15}$ powder after plasma spheroidization: (**a**) investigated area; (**b**) Ti; (**c**) Co; (**d**) Ni; (**e**) Cu; (**f**) Zr; (**g**) Hf; (**h**) Fe
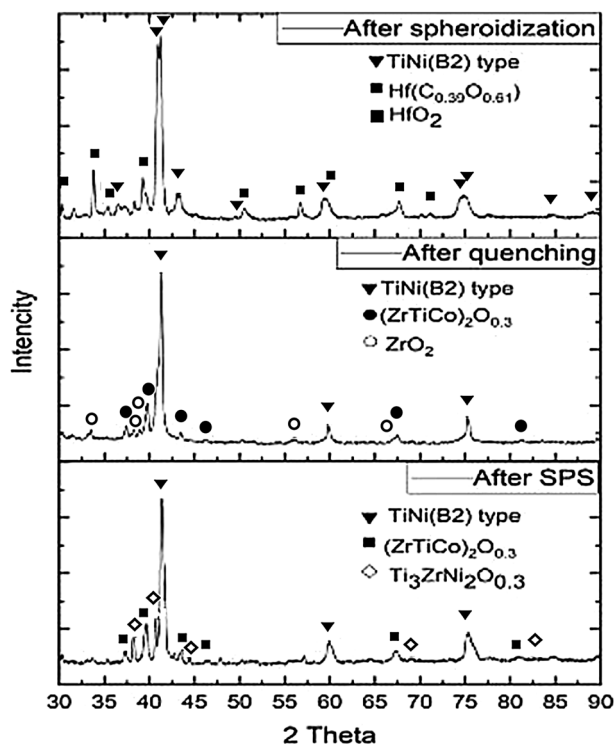
Fig. 7 Phase composition of HEA powders before and after plasma spheroidization, spark plasma sintering and quenching

solid solutions, notionally named $B2_1$ and $B2_2$) with well-defined, close to average lattice periods.

Table 1 shows the average chemical composition of the bulk HEA samples made by SPS process. The chemical composition almost coincides with the nominal composition of the powder obtained by mechanical alloying and plasma spheroidization that indicates a high degree of solubility of all the elements in the alloy. The Laves phase has a composition close to $(Zr, Hf)_7Cu_{10}$.
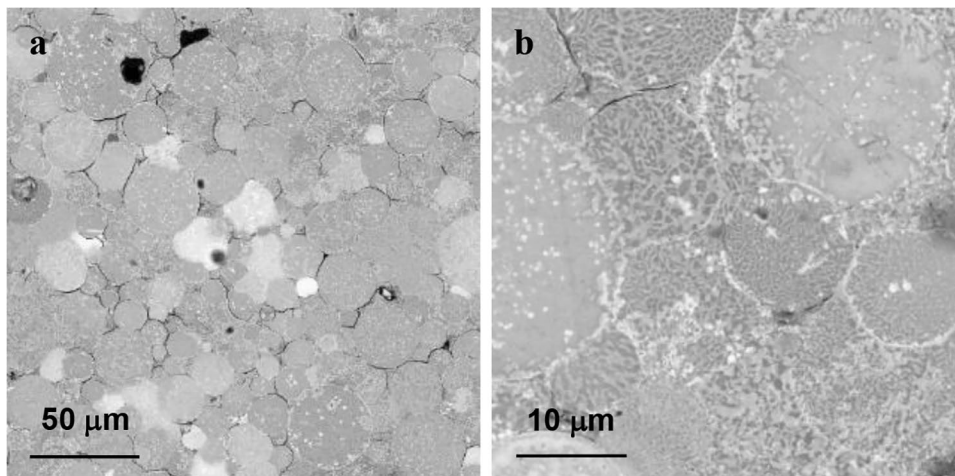
Table 2 and Fig. 10 show the results of mechanical compressive tests and hardness measurements for the bulk HEA samples obtained by SPS. The results showed that the bulk samples obtained by SPS have no plasticity. All samples were destroyed in the elastic deformation zone. This type of destruction is due to the fact that the adhesion of the initial powder particles occurs due to precipitation of the molten eutectic intermetallic phase and oxides along the boundaries. With this way to compact samples, the material does not work as a monolith sample.

Due to the high brittleness of the synthesized samples, it was not possible to test the functional properties characteristic of shape memory alloys, in particular, the martensitic transformation temperatures and reaction stresses, since the samples were destroyed in the holder even before the tests began.

Discussion

Analysis of the component distribution over the sample cross section after SPS (Fig. 9) showed that the distribution of elements in the B2 phase is almost homogeneous, and the Laves phase is enriched in Zr and Cu. The resulting Laves phase precipitated in the voids between the powder particles. The formation of microcracks along the interface between the particles of the initial powder and the resulting eutectic can be seen. This is probably due to the precipitation of oxide phases along the interface. The component distribution maps show the presence of oxygen which is consistent with the XRD results which established the presence of zirconium oxides ZrO and ZrO_2. A detailed study found that the highest oxygen content is concentrated at the boundaries of the resulting microcracks. The presence of the oxides in the resulting alloys can be explained by the content of undesirable impurities in the initial materials as well as by the absorption of the oxygen by the material during processing
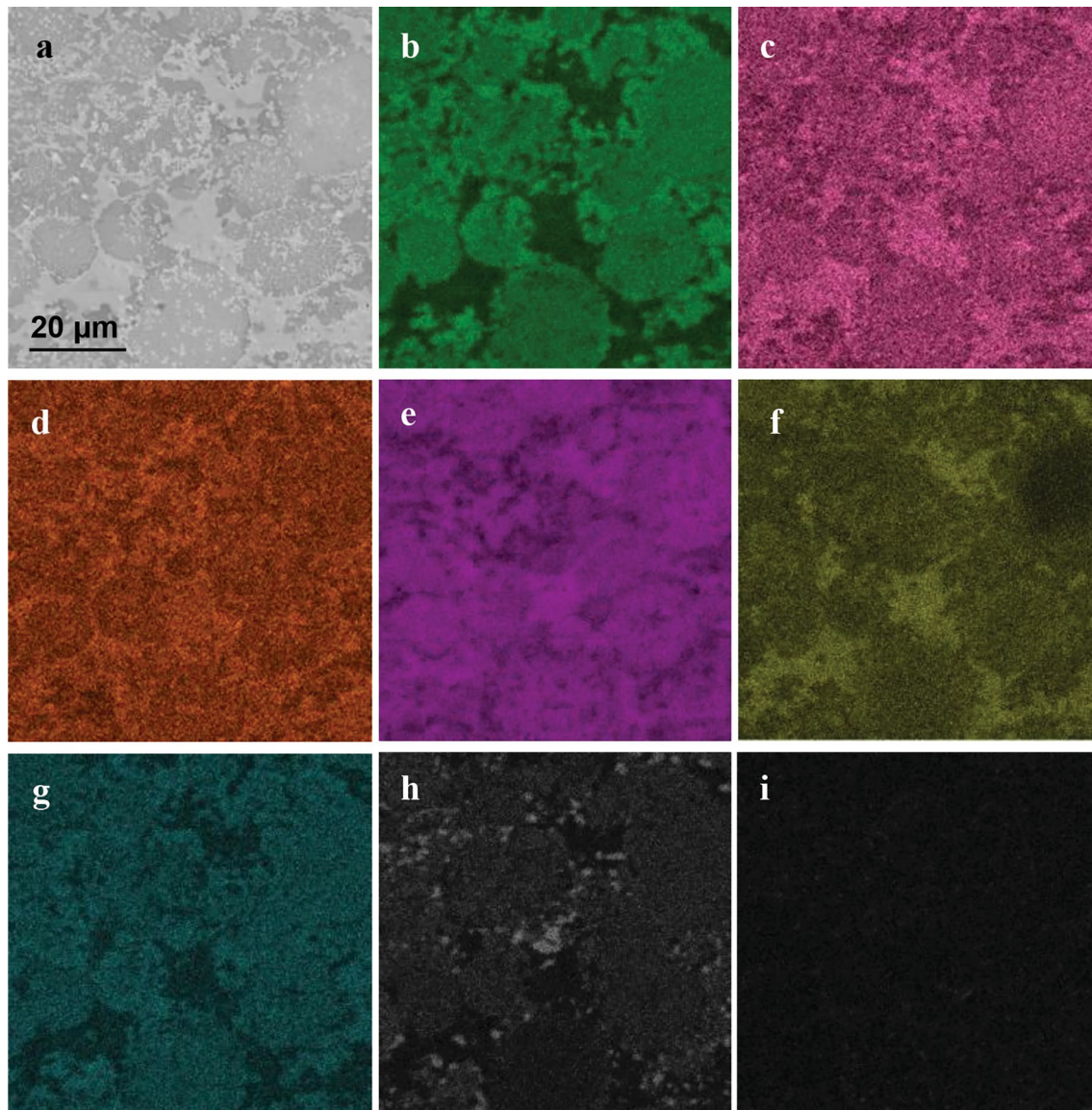
Fig. 8 Structure of bulk sample of $(TiZrHf)_{50}Ni_{25}Co_{10}Cu_{15}$ alloy obtained by SPS at various magnification: (**a**) 1000 ×; (**b**) 5000 ×

Fig. 9 Component distribution maps in bulk sample of $(TiZrHf)_{50}Ni_{25}Co_{10}Cu_{15}$ alloy obtained by SPS: (**a**) investigated area; (**b**) Ti; (**c**) Zr; (**d**) Hf; (**e**) Ni; (**f**) Cu; (**g**) Co; (**h**) Fe; (**i**) O

Table 1 Chemical composition (wt.%) of bulk sample of $(TiZrHf)_{50}Ni_{25}Co_{10}Cu_{15}$ alloy obtained by SPS

Sample name	Ti	Zr	Hf	Ni	Cu	Co	Fe
$(TiZrHf)_{50}Ni_{25}Cu_{15}Co_{10}$	22.97	13.32	19.34	26.95	6.52	6.88	4.01

because titanium and zirconium alloys are sensitive to even insignificant concentrations of oxygen in a low vacuum.

The analysis of the mechanical test results for the bulk HEA samples showed that the hardness of the synthesized samples was more than 600 HV which was significantly higher than for any single binary intermetallic such as TiCo, TiNi (250 HV), ZrCo (280 HV), HfCo (250–280 HV) and

corresponds to the hardness of HEAs of a similar composition obtained by conventional smelting technologies [42].

In addition to the influence of high distortions in the crystal lattice which lead to the implementation of solid-solution hardening mechanism, a sufficiently strong influence is exerted by Laves phase C15 precipitation. They both lead to a significant increase in the strength

Table 2 Mechanical characteristics of bulk HEA samples obtained by SPS

Sample name	Compressive strength, MPa	Vickers hardness, HV
$(TiZrHf)_{50}Ni_{25}Cu_{15}Co_{10}$ SPS	410	678.2
$(TiZrHf)_{50}Ni_{25}Cu_{15}Co_{10}$ SPS + quenching	440	701.8
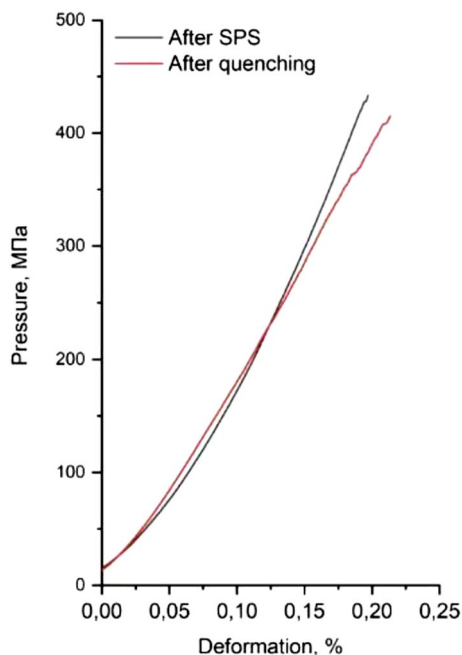
Fig. 10 Mechanical characteristics of bulk samples (TiZrHf)50Ni25Cu15Co10 alloy obtained by SPS

characteristics of $(TiZrHf)_{50}(NiCoCu)_{50}$ alloys. The Laves phases are formed when the difference between the largest and the smallest atomic radii of the elements included in the alloy is in range from 1.08 to 1.68. Its optimal value for the formation of the Laves phase C15 is 1.32 [43]. This value is 1.281 for the alloys of $(TiZrHf)_{50}(NiCoCu)_{50}$ type [42]. The relationship between the fraction of the formed phase and the content of Zr + Hf was revealed when analyzing the factors influencing the formation of C15 phase [42]. With an increase in the combined content of Zr and Hf, the proportion of the Laves phase C15 also increases from $1.7 \pm 0.2\%$ in the $Ti_{40}Zr_{10}Ni_{40}Co_5Cu_5$ alloy to $5.0 \pm 0.6\%$ in the equiatomic Ti-Zr-Hf-Ni-Co-Cu alloy $(Ti_{16.67}Zr_{16.67}Hf_{16.67}Ni_{16.67}Co_{16.67}Cu_{16.67})$.

With an increase in the difference in atomic radii and, as a result, with an increase in the lattice distortions, the strength of the alloy increases and its ductility decreases

that is consistent with the generally accepted material science data on the mechanical properties of metal alloys.

When analyzing the values of the compressive strength and plasticity of the synthesized SPS samples, it can be seen that they are very inferior to the samples obtained by conventional technologies. In particular, in [42], for $Ti_{30}Zr_{10}Hf_{10}Ni_{30}Co_{10}Cu_{10}$, $Ti_{20}Zr_{15}Hf_{15}Ni_{20}Co_{15}Cu_{15}$ and $Ti_{16.67}Zr_{16.67}Hf_{16.67}Ni_{16.67}Co_{16.67}Cu_{16.67}$ compositions, the ultimate strength is given in the range of 1590–2274 MPa. At the same time, the plasticity of the synthesized SPS samples is also significantly lower. In [42], it is from 0.63 to 3.8% for these alloys.

A significant deviation of the mechanical characteristics from the reference data is due to the presence of brittle Laves phases as well as to the high content of impurities (oxides) and the methods of making bulk samples. Oxygen is mainly concentrated at the boundaries of the powder particles as can be seen from the component distribution maps in the bulk samples. This can lead to brittle fracture along the boundaries of the particles under mechanical impact. Also, as a result of the SPS of $(TiZrHf)_{50}Ni_{25}Cu_{15}Co_{10}$ alloy, a low-melting point eutectic precipitated between the particles that is clearly seen in the SEM images of the sections of the bulk samples and according to the analysis of the chemical composition of the particles themselves and interparticle regions. This effect leads to the fact that the material does not work as a monolith and is destroyed at eutectic boundary at low loads and almost without plastic deformation.

In the references, there are the results of obtaining HEA with SME by vacuum melting methods which makes it possible to produce significantly cleaner alloys without impurities. The presence of the oxides in the alloys synthesized in this work can be explained by the content of undesirable impurities in the initial materials as well as by the absorption of the oxygen by the material during its subsequent processing. These facts indicate the further need to find a way to reduce the oxygen content at all stages of Ti-Zr-Hf-Ni-Co-Cu alloy synthesis because the powder metallurgy methods are of growing special interest to produce products of complex shape and composition with a large number of refractory elements.

Conclusion

When studying the bulk samples obtained by SPS from HEA powders synthesized by mechanical alloying and plasma spheroidization, it was found that during sintering a low-melting eutectic CuZr with melting point of 920 °C precipitated. The separation of the liquid phase prevents the deformation of the particles of the initial powder. It resulted to the conclusion that in the process of SPS the compaction occurs not due to interaction of the particles with each other but due

to connecting them by the melt of the low-melting eutectic. In the bulk sample, two-phase components different in contrast are found. The gray matrix has a phase structure corresponding to the austenitic state of B2-TiNi and the light gray inclusions have a structure corresponding to Laves phase. The data are confirmed by the XRD results. The average grain size of B2-austenite and Laves phase inclusions after SPS is ~ 2–3 μm. This structure corresponds to the structure of the initial powder which was formed during the plasma spheroidization process.

The hardness of the HEA samples is more than 600 HV which is significantly higher than for any single binary intermetallic such as TiCo, TiNi (250 HV), ZrCo (280 HV), HfCo (250–280 HV) and corresponds to the hardness of the HEA of a similar composition obtained by conditional smelting technologies.

The ultimate strength and plasticity are significantly lower than for similar alloys obtained by conventional methods because of the formation of eutectic between the particles and the oxygen concentration at the boundaries of the particles that have not melted during spark plasma sintering.

References

1. B. Cantor, I.T.H. Chang, P. Knight, A.J.B. Vincent, Microstructural development in equiatomic multicomponent alloys. Mater. Sci. Eng. A. **375–377**, 213–218 (2004). https://doi.org/10.1016/j.msea.2003.10.257

2. J.W. Yeh, S.K. Chen, S.J. Lin, J.Y. Gan, T.S. Chin, T.T. Shun, C.H. Tsau, S.Y. Chang, Nanostructured high-entropy alloys with multiple principal elements: novel alloy design concepts and outcomes. Adv. Eng. Mater. **6**, 299–303+274 (2004). https://doi.org/10.1002/adem.200300567.

3. D.B. Miracle, J.D. Miller, O.N. Senkov, C. Woodward, M.D. Uchic, J. Tiley, Exploration and development of high entropy alloys for structural applications. Entropy. **16**, 494–525 (2014). https://doi.org/10.3390/e16010494

4. Q. Wu, Z. Wang, F. He, L. Wang, J. Luo, J. Li, J. Wang, High entropy alloys: from bulk metallic materials to nanoparticles. Metall. Mater. Trans. A Phys. Metall. Mater. Sci. **49**, 4986–4990 (2018). https://doi.org/10.1007/s11661-018-4802-1

5. P. Sharma, V.K. Dwivedi, S.P. Dwivedi, Development of high entropy alloys: a review. Mater. Today Proc. **43**, 502–509 (2020). https://doi.org/10.1016/j.matpr.2020.12.023

6. T. Zhang, A. Inoue, Density, thermal stability and mechanical properties of Zr-Ti-Al-Cu-Ni bulk amorphous alloys with high Al plus Ti concentrations. Mater. Trans. **51**, 1494a–1494a (1998). https://doi.org/10.2320/matertrans.erm201001a

7. A. Inoue, Stabilization of metallic supercooled liquid and bulk amorphous alloys. Acta Mater. **48**, 279–306 (2000). https://doi.org/10.1016/S1359-6454(99)00300-6

8. M. Dada, P. Popoola, S. Adeosun, N. Mathe, High Entropy Alloys for Aerospace Applications, in *Aerodynamics*. [Working Title]. IntechOpen (2019), p. 13. https://doi.org/10.5772/intechopen.84982.

9. S. Praveen, H.S. Kim, High-entropy alloys: potential candidates for high-temperature applications—an overview. Adv. Eng. Mater. **20**, 1–22 (2018). https://doi.org/10.1002/adem.201700645

10. G. Qin, R. Chen, P.K. Liaw, Y. Gao, L. Wang, Y. Su, H. Ding, J. Guo, X. Li, An as-cast high-entropy alloy with remarkable mechanical properties strengthened by nanometer precipitates. Nanoscale. **12**, 3965–3976 (2020). https://doi.org/10.1039/c9nr08338c

11. J.-W. Yeh, Recent progress in high-entropy alloys. Ann. Chim. Sci. Des Matériaux. **31**, 633–648 (2006). https://doi.org/10.3166/acsm.31.633-648

12. J.-W. Yeh, Alloy design strategies and future trends in high-entropy alloys. JOM. **65**, 1759–1771 (2013). https://doi.org/10.1007/s11837-013-0761-6

13. G. Firstov, Y. Koval, J. van Humbeeck, A. Timoshevskii, T. Kosorukova, P. Verhovlyuk, Some physical principles of high temperature shape memory alloys design. Mater. Sci. Found. **81–82**, 207–231 (2015) https://doi.org/10.4028/www.scientific.net/msfo.81-82.207

14. G.S. Firstov, T.A. Kosorukova, Y.N. Koval, P.A. Verhovlyuk, Directions for high-temperature shape memory alloys' improvement: straight way to high-entropy materials? Shape Mem. Superelast. **1**, 400–407 (2015). https://doi.org/10.1007/s40830-015-0039-7

15. G. Firstov, A. Timoshevski, T. Kosorukova, Y. Koval, Y. Matviychuk, P. Verhovlyuk, Electronic and crystal structure of the high entropy TiZrHfCoNiCu intermetallics undergoing martensitic transformation. MATEC Web Conf. (2015). https://doi.org/10.1051/matecconf/20153306006

16. G.S. Firstov, T.A. Kosorukova, Y.N. Koval, V.V. Odnosum, High entropy shape memory alloys. Mater. Today Proc. **2**, S499–S503 (2015). https://doi.org/10.1016/j.matpr.2015.07.335

17. U. Icardi, L. Ferrero, Preliminary study of an adaptive wing with shape memory alloy torsion actuators. Mater. Des. **30**, 4200–4210 (2009). https://doi.org/10.1016/j.matdes.2009.04.045

18. J. Mohd Jani, M. Leary, A. Subic, M.A. Gibson, A review of shape memory alloy research, applications and opportunities. Mater. Des. **56**, 1078–1113 (2014). https://doi.org/10.1016/j.matdes.2013.11.084

19. М.Ю. Коллеров, Д.Е. Гусев, Г.В. Гуртовая, Н.В. Ручина, О.Н. Гвоздева, Функциональные материалы с эффектом памяти формы, Москва (2015)

20. K. Otsuka, X. Ren, Physical metallurgy of Ti-Ni-based shape memory alloys. Prog. Mater. Sci. **50**, 511–678 (2005). https://doi.org/10.1016/j.pmatsci.2004.10.001

21. D. Mantovani, Shape memory alloys: properties and biomedical applications. Jom. **52**, 36–44 (2000). https://doi.org/10.1007/s11837-000-0082-4

22. Е. Давыдов, А. Мушкин, И. Зуев, А. Ильин, М. Коллеров, Применение Биологически И Механически Совместимых Имплантатов Из Нитинола Для Хирургического Лечения Повреждений И Заболеваний Позвоночника И Спинного Мозга, Гений Ортопедии, 5–11 (2010)

23. J. Ma, I. Karaman, R.D. Noebe, J. Ma, I. Karaman, R.D. Noebe, High temperature shape memory alloys. Int. Mater. Rev. **55**, 257–315 (2010). https://doi.org/10.1179/095066010X12646898728363

24. Y.W. Kim, Shape memory characteristics and mechanical properties of powder metallurgy processed Ti50Ni40Cu10 alloy. J. Nanosci. Nanotechnol. **14**, 8061–8065 (2014). https://doi.org/10.1166/jnn.2014.9448

25. T.W. Duerig, A.R. Pelton, in *Materials Properties Handbook: Titanium Alloys*, ed. by R. Boyer, E.W. Collings, G. Welsch (ASM International, ASM World Headquarters, Materials Park, OH, 1994), pp. 1035–1048

26. K. Otsuka, X.B. Ren, Factors affecting the Ms temperature and its control in shape-memory alloys. Mater. Sci. Forum. **394–395**, 177–184 (2002) https://doi.org/10.4028/www.scientific.net/MSF.394-395.177

27. A. Bragov, A. Galieva, V. Grigorieva, A. Danilov, A. Konstantinov, A. Lomunov, A. Motorin, E. Ostropiko, A. Razov, Functional properties of TiNi shape memory alloy after high strain rate loading. Mater. Sci. Forum. **738–739**, 326–331 (2013) https://doi.org/10.4028/www.scientific.net/MSF.738-739.326

28. L.C. Zhang, L.Y. Chen, A review on biomedical titanium alloys: recent progress and prospect. Adv. Eng. Mater. **21**, 1–29 (2019). https://doi.org/10.1002/adem.201801215

29. H. Meier, C. Haberland, J. Frenzel, Structural and functional properties of NiTi shape memory alloys produced by Selective Laser Melting, in *Innovative Developments in Virtual and Physical Prototyping—Proceedings of 5th International Conference on Advanced Research in Virtual and Rapid Prototyping* (2012), 291–296.

30. W.C. Kim, Y.J. Kim, J.S. Kim, Y.S. Kim, M.Y. Na, W.T. Kim, D.H. Kim, Correlation between the thermal and superelastic behavior of Ni 50–x Ti 35 Zr 15 Cu x shape memory alloys. Intermetallics. **107**, 24–33 (2019). https://doi.org/10.1016/j.intermet.2019.01.005

31. D. Canadinc, W. Trehern, J. Ma, I. Karaman, F. Sun, Z. Chaudhry, Ultra-high temperature multi-component shape memory alloys. Scr. Mater. **158**, 83–87 (2019). https://doi.org/10.1016/j.scriptamat.2018.08.019

32. S.H. Hong, J.T. Kim, H.J. Park, Y.S. Kim, J.Y. Suh, Y.S. Na, K.R. Lim, C.H. Shim, J.M. Park, K.B. Kim, Influence of Zr content on phase formation, transition and mechanical behavior of Ni-Ti-Hf-Zr high temperature shape memory alloys. J. Alloys Compd. **692**, 77–85 (2017). https://doi.org/10.1016/j.jallcom.2016.09.023

33. G.S. Firstov, J. Van Humbeeck, Y.N. Koval, High-temperature shape memory alloys some recent developments. Mater. Sci. Eng. A. **378**, 2–10 (2004). https://doi.org/10.1016/j.msea.2003.10.324

34. T.A. Kosorukova, G. Gerstein, V.V. Odnosum, Y.N. Koval, H.J. Maier, G.S. Firstov, Microstructure formation in cast TiZrHf-CoNiCu and CoNiCuAlGaIn high entropy shape memory alloys: a comparison. Materials (Basel). (2019). https://doi.org/10.3390/ma1224227

35. H.-C. Lee, Y.-J. Chen, C.-H. Chen, Effect of solution treatment on the shape memory functions of (TiZrHf)50Ni25Co10Cu15 high

36. K.B. Park, J.Y. Park, Y. Do Kim, T.W. Na, C. Bin Mo, J.I. Choi, J. Choi, H.S. Kang, H.K. Park, Spark plasma sintering behavior of TaNbHfZrTi high-entropy alloy powder synthesized by hydrogenation-dehydrogenation reaction. Intermetallics. (2021). https://doi.org/10.1016/j.intermet.2020.107077

37. F. Lukac, R. Musalek, M. Vilemova, J. Cizek, J. Kuriplach, J. Straska, J. Zyka, J. Malek, Defects in the high entropy alloy HfNbTaTiZr prepared by spark plasma sintering, in *AIP Conference Proceedings*, vol. 2182 (2019). https://doi.org/10.1063/1.5135856.

38. N. Shkodich, A. Sedegov, K. Kuskov, S. Busurin, Y. Scheck, S. Vadchenko, D. Moskovskikh, Refractory high-entropy hftatinbzr-based alloys by combined use of ball milling and spark plasma sintering: effect of milling intensity. Metals (Basel). **10**, 1–15 (2020). https://doi.org/10.3390/met10091268

39. F. Lukac, M. Dudr, R. Musalek, J. Klecka, J. Cinert, J. Cizek, T. Chraska, J. Cizek, O. Melikhova, J. Kuriplach, J. Zyka, J. Malek, Spark plasma sintering of gas atomized high-entropy alloy HfNbTaTiZr. J. Mater. Res. **33**, 3247–3257 (2018). https://doi.org/10.1557/jmr.2018.320

40. F. Lukáč, M. Vilémová, M. Klementová, P. Minárik, T. Chráska, The origin and the effect of the fcc phase in sintered HfNbTaTiZr. Mater. Lett. **286**, 1–5 (2021). https://doi.org/10.1016/j.matlet.2020.129224

41. A. Kim, T. Makhmutov, N. Razumov, A. Silin, A. Popovich, J.N. Zhu, V. Popovich, Synthesis of NiTi alloy powders for powder-based additive manufacturing. Mater. Today Proc. **30**, 679–682 (2019). https://doi.org/10.1016/j.matpr.2020.01.521

42. C.H. Chen, Y.J. Chen, J.J. Shen, Microstructure and mechanical properties of (TiZrHf)50(NiCoCu)50 high entropy alloys. Met. Mater. Int. (2019). https://doi.org/10.1007/s12540-019-00383-3

43. G. Leitner, G.E.R. Schulze, Crystal chemical stability conditions for intermetallic compounds (I) frequency distributions of laves-phases. Krist. Tech. **6**, 449–463 (1971). https://doi.org/10.1002/crat.19710060402

entropy shape memory alloy. Entropy. **21**, 1–14 (2019). https://doi.org/10.2186/jjps.31.1354